Coupled Maxwell and time-dependent orbital-free density functional calculations

Cody Covington

Department of Chemistry, Austin Peay State University, Clarksville, Tennessee 37043, USA
and Department of Physics and Astronomy, Vanderbilt University, Nashville, Tennessee 37235, USA

Justin Malave

Department of Physics and Astronomy, Vanderbilt University, Nashville, Tennessee 37235, USA

Kálmán Varga [*]

Department of Physics and Astronomy, Vanderbilt University, Nashville, Tennessee 37235, USA

Coupled Maxwell and time-dependent orbital-free calculations are implemented and tested to describe the interaction of electromagnetic waves and matter. The currents and induced fields predicted by the orbital-free calculations are compared to time-dependent density functional calculations and very good agreement is found for various systems including jellium sheets, jellium spheres, atomistic sheets, and icosahedron clusters.

I. INTRODUCTION

Ground-state density functional theory (DFT) [1] Kohn-Sham (KS) [2] calculations are very successful in condensed matter physics, because they provide a reasonably accurate description of material properties in a computationally manageable way. Mostly these DFT calculations are based on KS orbitals and, albeit some approaches scale linearly with the number of orbitals [3,4] for certain systems, in general KS-orbital-based DFT has cubic scaling with respect to the system size. Orbital-free (OF) DFT [5–8] became an attractive alternative because its main variable is the electron density and it computationally scales linearly with system size. OFDFT has shown considerable success in million-atom material simulations of metals [8–10], warm dense matter [11,12], and quantum dots [13–17]. Computer codes for efficient implementation of OFDFT have also been developed [9,18–20].

OFDFT directly calculates the ground-state electron density, minimizing the energy functional without using KS orbitals. The minimization leads to a single Schrödinger-like equation. This equation contains a potential that is derived from the kinetic energy (KE) functional [21,22] to enforce the antisymmetry requirement of the many-electron wave function.

Time-dependent problems, e.g., calculation of electronic stopping power [12,23], spectra of clusters [19], and plasmonics [24–26], have been also studied with the "time-dependent" OF (TDOF) approach. In this case a single time-dependent Schrödinger equation has to be solved with the additional difficulty that the KE potential is time dependent [27].

The main difficulty of the OF calculations is finding the appropriate approximations for the kinetic energy functional.

The simplest approximations use local or semilocal expressions, where the energy density depends only on the density and its derivatives at one spatial point [28–33]. However, the local and semilocal KE functionals do not have the correct linear response properties. To correct this, nonlocal (or two-point) KE functionals were developed invoking the linear response of the noninteracting homogeneous electron gas [34–36]. These nonlocal KE functionals work well for a nearly free electron gas and were developed further for more complicated cases [37–40]. These functionals are computationally expensive because they depend explicitly on density at two spatially separated points. More recently, efficient alternatives based on a line integral representation of the KE functional have been proposed and tested [13,41,42]. While nonlocal functionals are considered to be superior, semilocal functionals are faster and new semilocal functionals have been developed that show very good accuracy [32,33]. Recent advances in machine learning techniques were also put to work in the quest for better KE functionals [20,43–46].

The development of dynamic KE functionals for time-dependent problems is less advanced than the static ones. In Ref. [27], a dynamic KE potential is proposed that is time propagated and forces the system to closely fit the susceptibility of the noninteracting homogeneous electron gas (Lindhard function) [47]. In Ref. [23] a local current density dynamic KE potential is derived by perturbation theory. This approach is computationally more efficient because it does not require the time propagation of the KE potential. Both approaches seem to reproduce the frequency-dependent Lindhard function nicely.

In this work we use the TDOF approach coupled with the Maxwell equations to describe the interaction of electromagnetic waves and matter. In a previous paper [48] we developed a method to solve the coupled Maxwell TDKS equations. In this coupled frame, the densities and current are calculated in

*kalman.varga@vanderbilt.edu

075119-1

a quantum-mechanical framework in the presence of a time-dependent vector potential and then the Maxwell equations are solved with the calculated time-dependent microscopic currents and densities to obtain the new vector potential. In order for the coupling of the quantum and Maxwell dynamics to be significant one needs large systems with many electrons. One can use time-dependent density functional theory (TDDFT) [49] (as we did in Ref. [48]), but that limits the application to relatively small systems. The OF approach allows the simulation of much larger systems (on the scale of millions of atoms [8–14]). The OF approach may allow for electrodynamic simulations to be performed for systems of relevant size with a quantum description of the electrons.

The goal of this paper is to implement coupled Maxwell TDOF calculations and test them against TDDFT results. We will solve the TDOF and TDDFT equations using a real-space grid and real-time propagation [50]. The Maxwell equations are solved using the Riemann-Silberstein formalism [48,51]. To make the TDOF and TDDFT calculations comparable we add a constraining potential to the TDOF Hamiltonian. This potential ensures that the initial ground-state densities are the same in the OF and DFT calculations.

II. FORMALISM

A. Time-dependent Kohn-Sham equations

The TDKS equation for the ith electron orbital is

$$\left(i\hbar\frac{\partial}{\partial t} - H_{\mathrm{KS}}\right)\psi_i(\mathbf{r}, t) = 0, \qquad (1)$$

where

$$H_{\mathrm{KS}}(\mathbf{r}, t) = -\frac{1}{2m}[-i\hbar\nabla_{\mathbf{r}} + \mathbf{A}(\mathbf{r}, t)]^2 + V_{\mathrm{KS}}(\mathbf{r}, t). \qquad (2)$$

The Kohn-Sham potential,

$$V_{\mathrm{KS}}(\mathbf{r}, t) = V_{\mathrm{ext}}(\mathbf{r}) + V_{\mathrm{H}}[\rho](\mathbf{r}) + V_{\mathrm{XC}}[\rho](\mathbf{r}), \qquad (3)$$

is a sum of the external potential, the Hartree, and the exchange-correlation terms. The vector potential, $\mathbf{A}(\mathbf{r}, t)$, describes the electromagnetic fields. The TDKS equations can be solved by time propagation and one can calculate the electron density and current at any time t as

$$\rho(\mathbf{r}, t) = 2\sum_{i=1}^{N_e/2} |\psi_i(\mathbf{r}, t)|^2. \qquad (4)$$

$$\mathbf{J}(\mathbf{r}, t) = 2\,\mathrm{Re}\sum_{i=1}^{N_e/2} [\psi_i(\mathbf{r}, t)^*(-i\hbar\nabla_{\mathbf{r}} + \mathbf{A}(\mathbf{r}, t))\psi_i(\mathbf{r}, t)]. \qquad (5)$$

where N_e is the number of electrons in the system and each orbital is occupied by two electrons. This current is input into the Maxwell equations, which will then propagate a vector potential $\mathbf{A}(\mathbf{r}, t)$.

B. Time-dependent orbital-free equations

The TDOF equation is

$$\left(i\hbar\frac{\partial}{\partial t} - H_{\mathrm{OF}}\right)\Psi(\mathbf{r}, t) = 0, \qquad (6)$$

where

$$H_{\mathrm{OF}}(\mathbf{r}, t) = -\frac{1}{2m}[-i\hbar\nabla_{\mathbf{r}} + \mathbf{A}(\mathbf{r}, t)]^2 + V_{\mathrm{OF}}(\mathbf{r}, t). \qquad (7)$$

The orbital-free potential is defined as

$$V_{\mathrm{OF}}(\mathbf{r}, t) = V_{\mathrm{KS}}(\mathbf{r}) + V_{\mathrm{TF}}[\rho](\mathbf{r}) + (a - 1)V_{\mathrm{W}}[\rho](\mathbf{r}) + V_{\mathrm{c}}(\mathbf{r}), \qquad (8)$$

where V_{TF} is the Thomas-Fermi kinetic energy functional, V_{W} is the von Weizsäcker potential, and V_{c} is a constraining potential that we will define later. a is a numerical coefficient of the Weizsäcker term. Normally the Weizsäcker term comes with an "a" multiplier (with values $a = 1$ to $1/9$). Here $a - 1$ appears because the 1 has to compensate the appropriate part in the kinetic energy in Eq. (6). In this case the electron density and current at any time t are

$$\rho_{\mathrm{OF}}(\mathbf{r}, t) = |\Psi(\mathbf{r}, t)|^2, \qquad (9)$$

$$\mathbf{J}_{\mathrm{OF}}(\mathbf{r}, t) = 2\,\mathrm{Re}\,[\Psi(\mathbf{r}, t)^*(-i\hbar\nabla_{\mathbf{r}} + \mathbf{A}(\mathbf{r}, t))\Psi(\mathbf{r}, t)]. \qquad (10)$$

C. Constrained minimization

To compare TDDFT and OF one ideally would use the same ground-state density, but V_{KS} and V_{OF} produce different densities, $\rho(\mathbf{r})$ and $\rho_{\mathrm{OF}}(\mathbf{r})$, respectively. In Ref. [52] we have presented a constrained density functional approach. This method can be used to generate a constraining potential that forces the charge density to be equal to a prescribed density. In the present case we use the constraint

$$|\Psi(\mathbf{r})|^2 = \rho(\mathbf{r}), \qquad (11)$$

where $\rho(\mathbf{r})$ is the density of the ground-state DFT calculation.

The following iterative procedure can be used to calculate the constraining potential:

$$\Psi^{(n+1)}(\mathbf{r}) = \Psi^{(n)}(\mathbf{r}) - x_0(\hat{H}_{\mathrm{OF}} + \lambda^{(n)}\hat{Q} - \epsilon^{(n)})\Psi^{(n)}(\mathbf{r}), \qquad (12)$$

where x_0 controls the convergence,

$$\epsilon^{(n)} = \langle\Psi^{(n)}|H_{\mathrm{OF}}|\Psi^{(n)}\rangle \qquad (13)$$

is the energy expectation value, and $\hat{Q}$ is the density operator such that

$$\langle\Psi^{(n)}|\hat{Q}|\Psi^{(n)}\rangle = |\Psi^{(n)}(\mathbf{r})|^2. \qquad (14)$$

Given a desired initial density distribution $\rho(\mathbf{r})$ one looks for the potential $\lambda(\mathbf{r})$,

$$\lambda(\mathbf{r})\psi^{(n)}(\mathbf{r}) = \lambda\hat{Q}\psi^{(n)}, \qquad (15)$$

which constrains the density according to Eq. (11).

The constrained minimization allows us to construct an orbital-free Hamiltonian, H_{OF}, that produces the same self-consistent potential and density as the TDDFT calculation. In this way the TDDFT and the OF calculations can be directly compared. Since the constrained ground-state density is the same, by setting

$$V_c(\mathbf{r}) = \lambda(\mathbf{r}), \qquad (16)$$

the contributions to the energy from the potentials are the same:

$$\langle \Psi | V_{OF} | \Psi \rangle = 2 \sum_{i=1}^{N/2} \langle \psi_i | V_{KS} | \psi_i \rangle. \qquad (17)$$

The kinetic energy parts in OF,

$$\langle \Psi | \frac{\hbar^2}{2m} \nabla_{\mathbf{r}}^2 | \Psi \rangle, \qquad (18)$$

and in TDDFT,

$$2 \sum_{i=1}^{N/2} \langle \psi_i | \frac{\hbar^2}{2m} \nabla_{\mathbf{r}}^2 | \psi_i \rangle, \qquad (19)$$

are different, although in numerical calculations the difference is small. The constraining potential forces a match of the ground-state OF density to the DFT density, and is then applied the OF Hamiltonian. The constraining potential is kept fixed during the time evolution in these calculations.

D. The Riemann-Silberstein formalism

In a previous paper [48] we developed an approach to solve the coupled Maxwell TDKS equations in a numerically efficient way using the Riemann-Silberstein formalism. The Riemann-Silberstein (RS) vector is defined as

$$\mathbf{F}(\mathbf{r}, t) = \sqrt{\frac{\epsilon_0}{2}} \mathbf{E}(\mathbf{r}, t) \pm i \sqrt{\frac{1}{2\mu_0}} \mathbf{B}(\mathbf{r}, t),$$

where **B** and **E** are magnetic and electric fields. In this formalism the Maxwell equations can be rewritten in the form

$$\nabla \cdot \mathbf{F} = \frac{1}{\sqrt{2\epsilon_0}} \rho$$

and

$$i\hbar \frac{\partial \mathbf{F}}{\partial t} = c \left(\mathbf{S} \cdot \frac{\hbar}{i} \nabla_{\mathbf{r}} \right) \mathbf{F} - \frac{i\hbar}{\sqrt{2\epsilon_0}} \mathbf{J}, \qquad (20)$$

where **S** are 3×3 the spin-1 Pauli matrices. The attractive feature of this formalism is that Eq. (20) is similar to a time-dependent Schrödinger equation and can be solved with time-propagation approaches used in quantum mechanics. As it is described in detail in Ref. [48], the Helmholtz decomposition of the Riemann-Silberstein vector allows the removal of the longitudinal component which is responsible for the Hartree potential. The Hartree potential is calculated by solving the Poisson equation using the electron density as it is standard in the conventional DFT calculations. Further details of coupling the Maxwell equations to the TDDFT Hamiltonian are given in Refs. [51,53].

To solve the Maxwell equation the electron density and current are calculated by solving the TDKS or TDOF equations and then used to calculate **F** at time $t + \Delta t/2$. Once **F** is known, the vector potential, **A**, at $t + \Delta t$ needed in the quantum equations can be calculated from **E** in a leapfrog algorithm [48].
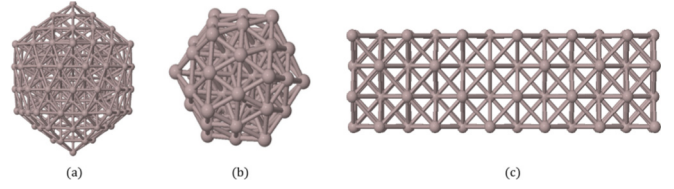

FIG. 1. Side view (*xy* plane) of nanoclusters and metal sheets used in the calculations: (a) Al_{147} and (b) Al_{55} icosahedrons and (c) Al thin film. The laser propagates in the *x* direction. In the case of Al thin film the system is periodic in the *y* and *z* directions.

III. RESULTS

In this section we present test calculations comparing Maxwell TDDFT and Maxwell TDOF calculations. Taylor time propagation is used to solve the TDKS [Eq. (1)] and TDOF [Eq. (6)] equations. The time step in the time evolution of these equations is $\Delta t = 0.02$ a.u., and the time step in the propagation of the RS vector [Eq. (20)] is $\Delta t/20$. The TDKS and the TDOF equations are solved on a numerical grid using a nine-point finite difference representation for the kinetic energy [50]. The grid spacing is $\Delta x = \Delta y = \Delta z = 0.5$ for both jellium and for systems with atoms. The number of grid points is $N = N_x \times N_y \times N_z$, where N_i is the number of grid points in the $i = x, y, z$ directions. The RS equations are solved in Fourier space [48] corresponding to the same grid. The local density approximation is used for the exchange-correlation potential [54] and the pseudopotential for Al is taken from Ref. [55]. Free or periodic boundary conditions (PBCs) are used in different directions as indicated in the examples. To avoid reflection of wave functions or electromagnetic waves, complex absorbing potentials (CAPs) are added at the boundary. The same CAP is used as in Ref. [48]. Examples of system geometries are shown in Fig. 1.

The first step of the approach is a ground-state DFT calculation to determine the initial wave function and initial density. Figure 2 compares the ground-state density of the DFT and the OF calculation for an Al_{55} icosahedron cluster with 165 electrons, using a geometry that is adapted from Ref. [56]. To compare the ground-state densities between DFT and the OF calculations, the orbital-free density was not constrained in this case, i.e., $V_c = 0$. The densities of the DFT and the OF calculations are very close, but slight differences in the density cause a large difference in the potential (Fig. 2 shows the magnitude of the necessary constraining potential) and in the energy.

In the second step a constrained minimization is used to generate a potential, V_c, that forces the OF calculation to produce the same density as ρ, the density obtained by the DFT calculation. In this step we require

$$|\rho(\mathbf{r}) - \rho_{OF}(\mathbf{r})| < \epsilon, \qquad (21)$$

with $\epsilon = 10^{-6}$. We start with V_{OF}, Ψ, and ρ_{OF} calculated in the OF calculation, setting $V_c = 0$. Then we set $\Psi^{(1)} = \Psi$, $\lambda^{(1)} = 0$ and use the iteration defined in Eq. (12) to calculate $\Psi^{(n+1)}$. The confining potential is updated in each step as $V_c(\mathbf{r}) = \lambda^{(n)}(\mathbf{r})$.

The calculated V_c is shown in Fig. 2. Using this constraining potential in V_{OF} one gets exactly the same self-consistent
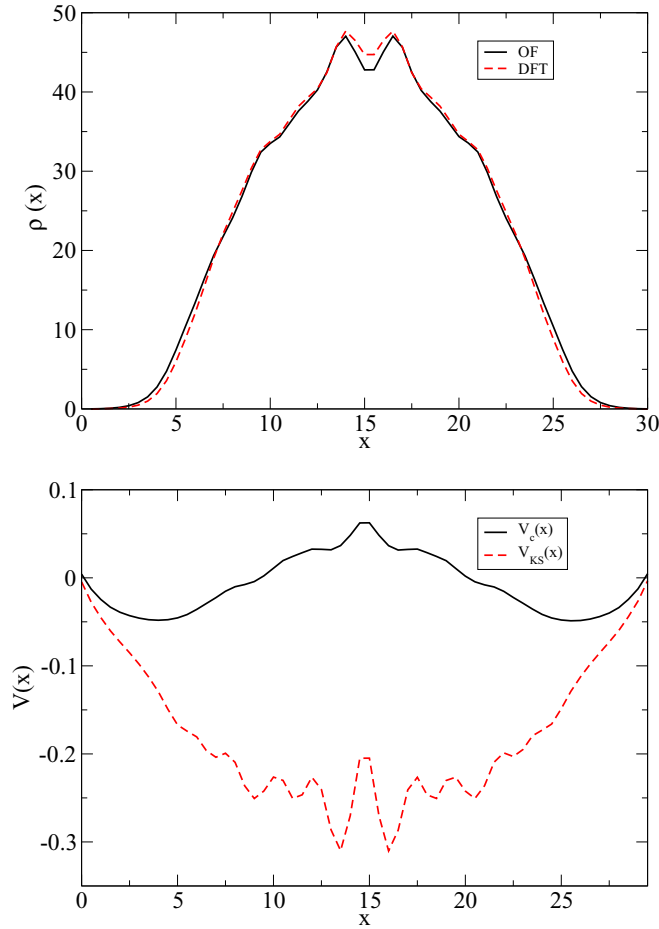
FIG. 2. Density and potential profile of an Al$_{55}$ cluster with 164 electrons. $N_x = N_y = N_z = 60$ grid points used in the calculation. Top: Comparison of the unconstrained-OF and DFT electron densities averaged along the x direction, $\rho(x) = \sum_{y,z} \rho(\mathbf{r})$. Bottom: The confining and the KS potential averaged along the x direction, $V(x) = \frac{1}{N_y N_z} \sum_{y,z} V(\mathbf{r})$.

density in the OF and DFT calculations. The constraining potential is positive in the middle, decreasing the OF density to make it closer to DFT, and negative away from the center to pull the OF density closer to that of DFT. To study the time-dependent behavior of the density in TDDFT and OF in this case we have calculated the time dependence of the dipole moment. To start the calculation the initial ground-state wave functions were perturbed by multiplying them with e^{ikx}, with $k = 0.01$ a.u. and the systems were time propagated up to $T = 500$ a.u. The calculated dipole moment $d(t) = \int \rho(\mathbf{r}, t) x d\mathbf{r}$ is shown in Fig. 3. The TDDFT and OF dipole moments are very close to each other in the beginning of the calculation, but later the oscillations are different. It seems that the constraining potential works well in the initial stage of the time propagation, but later dynamical effects become important. This can probably be improved by invoking a dynamical kinetic energy potential [27,57]. The frequency of the oscillation of the dipole moment remains very similar in the OF and TDDFT calculations and the resulting absorption spectra are similar (see Fig. 3). The usefulness of the OF approach for the calculation of the absorption spectrum of quantum dots using a dynamical kinetic energy functional has been discussed in Refs. [24,26].
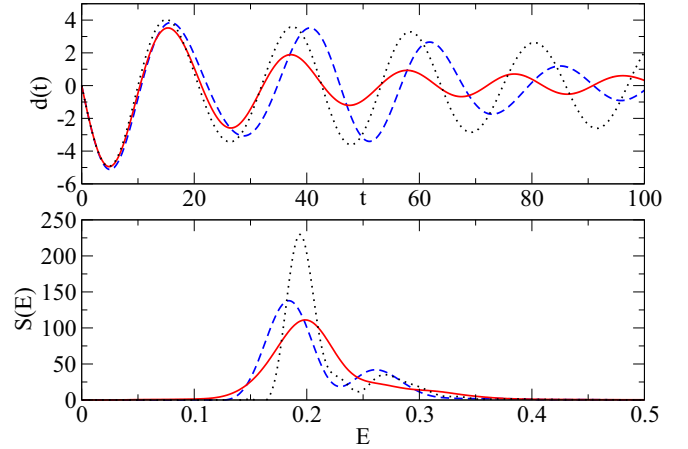

FIG. 3. Time dependence of the dipole moment and the absorption spectrum of an Al$_{55}$ cluster (solid line, TDDFT; dashed line, TDOF). Please see Fig. 2 for details of the calculation. The absorption spectrum is defined as $\alpha(E) = \frac{e^2}{k\hbar} \int (d(t) - d(0)) e^{iEt/\hbar} g(t) dt$, where $g(t)$ is a damping function. The dotted line shows the TDOF results starting from the OF density (without constraining potential). In this case the starting density, potential, and energy are different from the TDDFT case and the comparison is more difficult.

To test the coupled Maxwell-TDOF calculations we compare them to coupled Maxwell-TDDFT calculations. First, we use three test cases from Ref. [48]. In the first case, an electromagnetic pulse excites a jellium sheet. Because the Maxwell equations are linear, the electric field can be written as the sum of an external field and an induced field created by the electron currents, $\mathbf{E}_{tot} = \mathbf{E}_{ext} + \mathbf{E}_{ind}$. In this way, the exciting pulse does not need a source and never has to be time propagated because its form is analytic. The external field is given as a Gaussian laser pulse ($\mathbf{E}_{ext}$ in Fig. 4):

$$\mathbf{E}_{ext}(\mathbf{r}, t) = \left(0, 0, E_0 e^{-(t-t_0-x/c)^2/\alpha^2}\right). \quad (22)$$

Here t_0 is the pulse shift, and α controls the width of the pulse.

To show the time dependence of the electric field and currents we define the average electric field as

$$\mathbf{E}(t) = \frac{1}{N} \sum_{\mathbf{r}} \mathbf{E}(\mathbf{r}, t), \quad (23)$$

and

$$\mathbf{J}(t) = \frac{1}{N} \sum_{\mathbf{r}} \mathbf{J}(\mathbf{r}, t), \quad (24)$$

where the sum is over grid points that are not in the CAP region. In the figures only the z components $E = E_z$ (for $\mathbf{E}_{tot}$, $\mathbf{E}_{ext}$, and $\mathbf{E}_{ind}$) and $J = J_z$ are shown.

Figure 4(a) shows the induced currents for coupled and uncoupled cases. In the uncoupled case, the Maxwell equations are not time propagated and $\mathbf{E}_{tot} = \mathbf{E}_{ext}$. For the coupled case, the Maxwell equations are time propagated and the currents produce an induced field opposite to $\mathbf{E}_{ext}$. It is this induced field that deexcites the electrons and causes the current to fall back to zero. The results of the TDDFT and TDOF calculations agree up to four significant digits for the induced
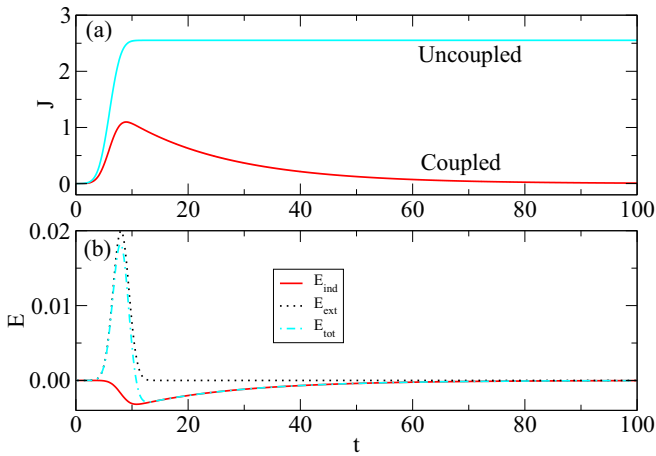
FIG. 4. Comparison of TDOF and TDDFT simulations showing the averaged currents (top) and the electric fields (bottom). The system is lithium jellium consisting of 36 electrons in a 328-a.u.-wide sheet contained within a box of $N_x = 1152$, $N_y = N_z = 8$. CAPs were used in the x direction and PBCs were used in the y and z directions. The system was excited by a Gaussian pulse with a peak electric field of $E_0 = 0.02$ a.u., a width of $\alpha = 2.0$ a.u. and a shift of $t_0 = 6$ a.u. The results of the TDDFT and TDOF calculations agree up to four significant digits for the induced currents and induced fields, making the TDDFT and TDOF calculations indistinguishable.

currents and induced fields and one cannot distinguish the results in Fig. 4.

The perfect agreement is very surprising considering that 18 orbitals are time propagated in TDDFT and only one in TDOF. We see later that this agreement is mostly due to symmetry of the jellium sheet system. Figure 4(a) also shows that in the uncoupled case the system stays in an excited state
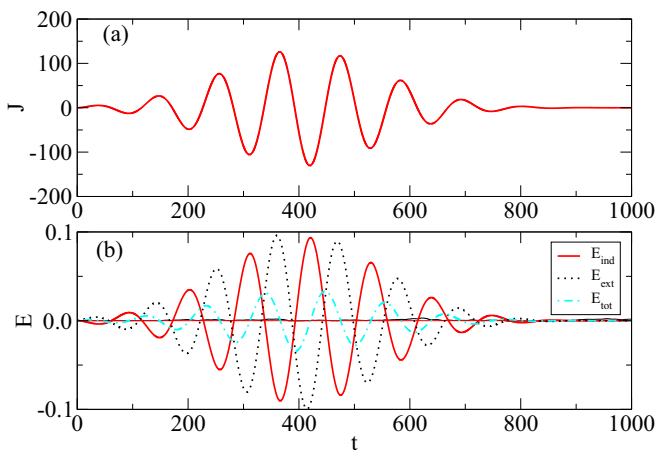

FIG. 5. Calculated currents and induced fields in the case of a laser pulse incident from the left on a 232-a.u.-thick sheet of aluminum jellium of 400 electrons within a box of $N_x = 640$, $N_y = N_z = 16$. Also in this case the OF and TDDFT curves are on top of each other. CAPs were used in the x direction and PBCs were used in the y and z directions. The system was excited by a Gaussian pulse with a peak electric field of $E_0 = 0.1$ a.u., a width of $\alpha = 206$ a.u., $\omega = 0.05695$ a.u., and a shift of $t_0 = 400$ a.u.
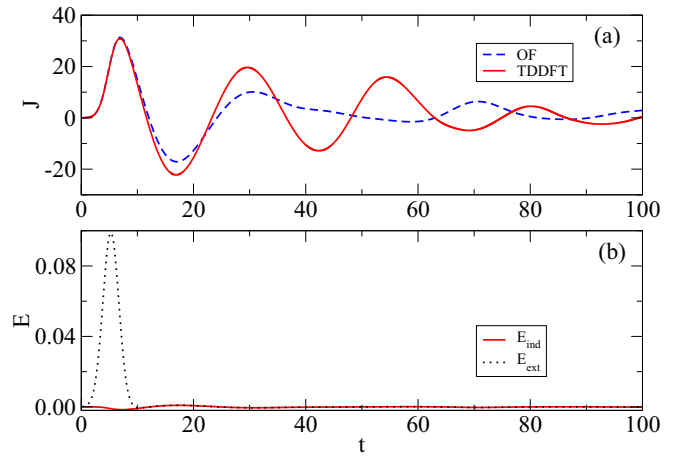

FIG. 6. Comparison of the cell average currents in time resulting from a strong laser pulse incident from the left on a sphere of aluminum jellium of 236 electrons in a box of $N_x = 192$ a.u., $N_y = N_z = 60$ a.u. CAPs were used in the x direction and PBCs were used in the y and z directions. The system was excited by a Gaussian pulse with a peak electric field of $E_0 = 0.1$ a.u. with a width of $\alpha = 2$ a.u. and a shift of $t_0 = 5$ a.u.

while in the coupled case the system relaxes to the ground state and the electric current decreases to zero.

In the second test case (see Fig. 5) a sheet of aluminum jellium is irradiated with a laser pulse of the form

$$\mathbf{E}_{\text{ext}}(\mathbf{r}, t) = (0, 0, E_0 e^{-(t-t_0-x/c)^2/\alpha^2} \sin(\omega(t - x/c))). \quad (25)$$

The TDDFT and OF currents and induced electric fields are in perfect agreement, up to three significant digits. In this case the electric field penetrates the thick Al sheet, generating strong currents. Still, the results of the TDDFT calculations with 200 orbitals and the orbital-free calculation are the same.

In the third example, a jellium sphere of radius 12.8 a.u. containing 236 electrons is used with a short Gaussian pulse (see Fig. 6). In this case the induced electric field is negligible. The OF and TDDFT currents are very close to each other during the laser pulse, but after the excitation the time
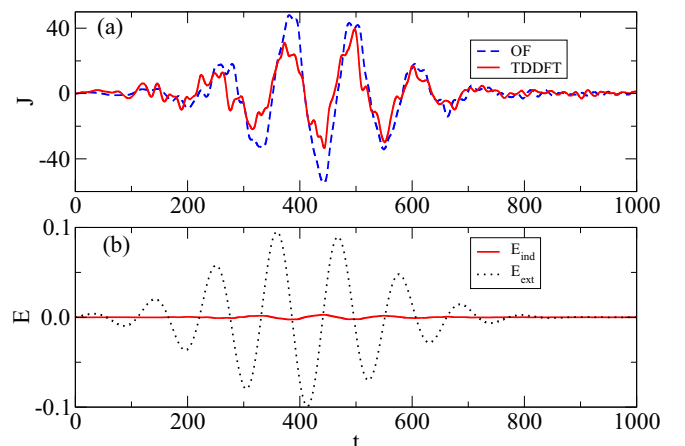

FIG. 7. The same system as described in the caption of Fig. 6 but with the laser pulse of Fig. 5.
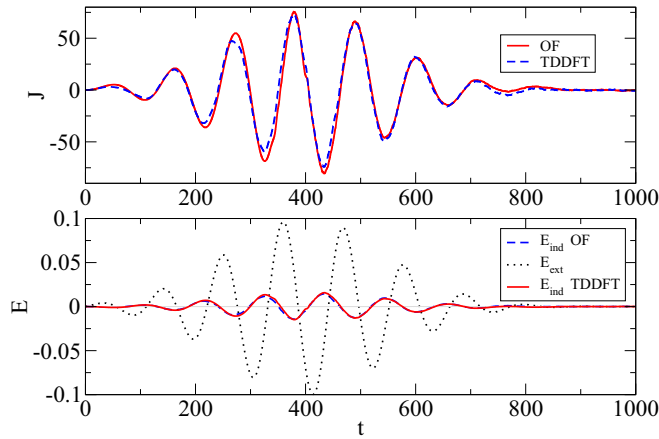
FIG. 8. Comparison of OF and TDDFT currents and induced electric fields in a 36-atom, 96-electron Al sheet. $N_x = 200$, $N_y = N_z = 31$, and $\Delta_x = \Delta_y = \Delta_z = 0.4932$ a.u. are used. A CAP is added in the x direction and PBCs in the y and z directions. The parameters of the laser field are given in the caption of Fig. 5.

dependence of the currents is different. The same system with the longer pulse is shown in Fig. 7. The OF and TDDFT are not in perfect agreement as before, but they are similar and they follow the external pulse with the same delay time. This test shows the role of symmetry, comparing a sheet and a spherical jellium system. One can cut the sphere into n slices in parallel with the direction of the laser. The currents and density oscillations will be different in each slice depending on their diameter. In the jellium sheet cases the response is the same in each slice. Additionally, the jellium sphere presents a surface which causes reflections of the electron density driven to the surface by the laser field. In the case of TDDFT, there are 118 orbitals with different energies and different reflections. For larger systems the effect of the surface is expected to be smaller.
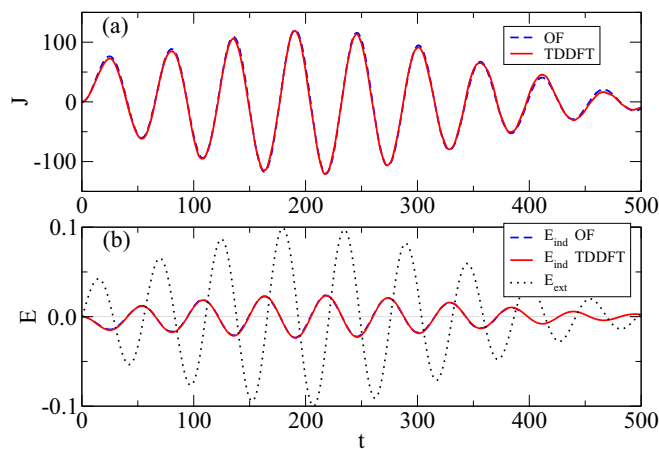

FIG. 9. Comparison of OF and TDDFT currents and induced electric fields in a 96-atom, 288-electron Al sheet. $N_x = 200$, $N_y = N_z = 31$, and $\Delta_x = \Delta_y = \Delta_z = 0.4932$ a.u. are used. A CAP is added in the x direction and PBCs in the y and z directions. The laser pulse has a peak electric field of $E_0 = 0.1$ a.u., a width of $\alpha = 200$ a.u., $\omega = 0.1139$ a.u., and a shift of $t_0 = 200$ a.u.
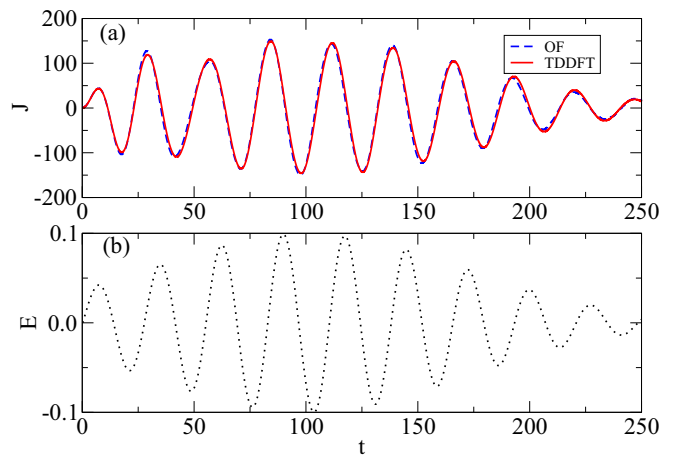

FIG. 10. Comparison of OF and TDDFT currents in a 147-atom icosahedron Al cluster with 440 electrons. The number of grid points is $N_x = 200$, $N_y = N_z = 60$, and a CAP is added in the x direction and free boundary conditions are used in the y and z directions. The laser pulse has a peak electric field of $E_0 = 0.1$ a.u., a width of $\alpha = 100$ a.u., $\omega = 0.2278$ a.u., and a shift of $t_0 = 100$ a.u.

Next we present examples with atoms. In Figs. 8 and 9 OF and TDDFT calculations of a 32-atom and 96-atom Al sheets are compared. The agreement of the OF and TDDFT results is excellent; the thicker (the width is about 42 a.u.) sheet of the 96-atom system has better agreement than the thinner case. This example illustrates that the presence of atomic potentials does not greatly affect the agreement between the OF and TDDFT results.

Finally, we present a calculation for an Al_{147}^+ icosahedron cluster (see Fig. 10). As the TDDFT calculations are computationally demanding, we use a shorter pulse in this case. The coupling to the Maxwell equations is also turned of, partly to increase the speed of the calculation and partly because the induced fields are small as we have seen in the jellium case (see Fig. 7). The agreement of the TDDFT and OF calculations is perfect. The reason for the very good agreement is probably due to the localization of the density by the atomic potentials. In the jellium case, the electron density is more easily moved by the field.

IV. SUMMARY

We have implemented and tested the coupled Maxwell and TDOF calculations to study the interaction of electromagnetic fields and matter. Nanometer- sized sheets and clusters were subject to short laser pulses and the induced currents and electric fields were compared to the result of TDDFT calculations. The results are in very good agreement, especially for larger systems. The examples and tests include dipole oscillation due to an instantaneous kick perturbation, excitation with a laser field, and coupled Maxwell and quantum dynamics. The coupled Maxwell case is a rigorous test because the system does not just follow the dynamics of the laser field but builds up a nonlinear response. This test is also important for possible applications. In the examples we have used a relatively strong electric field in the nonlinear region. We

have made many test calculations with weaker fields and the agreement between TDOF and TDDFT is even better in those cases.

The OF calculations have some limitations for smaller quantum dots [15–17] and the disagreement can perhaps be reduced by using more recently proposed kinetic energy functionals [13,14]. In these calculations, a constraining potential was used to force the OF ground-state density to match the DFT ground-state density. This step can probably be eliminated by using new generations of kinetic energy functionals [13,13,14,41,42,58].

Another potential improvement is using dynamic kinetic energy potentials [23,27]. These potentials have been tested only in very few cases and further development and tests might be needed.

In the present work the size of the studied systems is relatively small because TDDFT calculations are not feasible for larger systems. The results are promising and larger, physically more relevant systems will be studied in later works. The calculations presented in this work are also restricted to simple electronic structures and further studies for more complicated cases, e.g., Mg metal clusters, are necessary in the future.

[1] P. Hohenberg and W. Kohn, Phys. Rev. **136**, B864 (1964).

[2] W. Kohn and L. J. Sham, Phys. Rev. **140**, A1133 (1965).

[3] S. Goedecker, Rev. Mod. Phys. **71**, 1085 (1999).

[4] D. R. Bowler and T. Miyazaki, Rep. Prog. Phys. **75**, 036503 (2012).

[5] Y. A. Wang and E. A. Carter, in *Theoretical Methods in Condensed Phase Chemistry*, edited by S. D. Schwartz (Kluwer Academic, Dordrecht, 2002), pp. 117–184.

[6] *Recent Progress in Orbital-Free Density Functional Theory*, edited by T. A. Wesolowski and Y. A. Wang (World Scientific, Singapore, 2013).

[7] V. V. Karasiev, D. Chakraborty, and S. Trickey, in *Many-Electron Approaches in Physics, Chemistry, and Mathematics*, edited by L. Delle Site and V. Bach (Springer, Heidelberg, 2014), pp. 113–134.

[8] W. C. Witt, B. G. del Rio, J. M. Dieterich, and E. A. Carter, J. Mater. Res. **33**, 777 (2018).

[9] X. Shao, Q. Xu, S. Wang, J. Lv, Y. Wang, and Y. Ma, Comput. Phys. Commun. **233**, 78 (2018).

[10] L. Hung and E. A. Carter, Chem. Phys. Lett. **475**, 163 (2009).

[11] T. G. White, S. Richardson, B. J. B. Crowley, L. K. Pattison, J. W. O. Harris, and G. Gregori, Phys. Rev. Lett. **111**, 175002 (2013).

[12] Y. H. Ding, A. J. White, S. X. Hu, O. Certik, and L. A. Collins, Phys. Rev. Lett. **121**, 145001 (2018).

[13] W. Mi and M. Pavanello, Phys. Rev. B **100**, 041105(R) (2019).

[14] X. Shao, W. Mi, and M. Pavanello, arXiv:2010.07385.

[15] G. S. Ho, C. Huang, and E. A. Carter, Curr. Opin. Solid State Mater. Sci. **11**, 57 (2007).

[16] A. Aguado, Phys. Rev. B **63**, 115404 (2001).

[17] A. Aguado, J. M. López, J. A. Alonso, and M. J. Stott, J. Phys. Chem. B **105**, 2386 (2001).

[18] M. Chen, J. Xia, C. Huang, J. M. Dieterich, L. Hung, I. Shin, and E. A. Carter, Comput. Phys. Commun. **190**, 228 (2015).

[19] X. Shao, K. Jiang, W. Mi, A. Genova, and M. Pavanello, WIREs Comput. Mol. Sci. **11**, e1482 (2021).

[20] P. Golub and S. Manzhos, Comput. Phys. Commun. **256**, 107365 (2020).

[21] A. Holas and N. H. March, Phys. Rev. A **44**, 5521 (1991).

[22] H. Levämäki, A. Nagy, K. Kokko, and L. Vitos, Phys. Rev. A **90**, 062515 (2014).

[23] A. J. White, O. Certik, Y. H. Ding, S. X. Hu, and L. A. Collins, Phys. Rev. B **98**, 144302 (2018).

[24] H. Xiang, M. Zhang, X. Zhang, and G. Lu, J. Phys. Chem. C **120**, 14330 (2016).

[25] H. Xiang, Z. Wang, L. Xu, X. Zhang, and G. Lu, J. Phys. Chem. C **124**, 945 (2020).

[26] H. Xiang, X. Zhang, D. Neuhauser, and G. Lu, J. Phys. Chem. Lett. **5**, 1163 (2014).

[27] D. Neuhauser, S. Pistinner, A. Coomar, X. Zhang, and G. Lu, J. Chem. Phys. **134**, 144101 (2011).

[28] M. Levy and Ou-Yang Hui, Phys. Rev. A **38**, 625 (1988).

[29] V. V. Karasiev, T. Sjostrom, and S. B. Trickey, Phys. Rev. B **86**, 115101 (2012).

[30] K. Luo, V. V. Karasiev, and S. B. Trickey, Phys. Rev. B **98**, 041111(R) (2018).

[31] L. A. Constantin, E. Fabiano, and F. Della Sala, J. Chem. Theory Comput. **15**, 3044 (2019).

[32] L. A. Constantin, E. Fabiano, and F. Della Sala, J. Phys. Chem. Lett. **9**, 4385 (2018).

[33] J. Lehtomäki and O. Lopez-Acevedo, Phys. Rev. B **100**, 165111 (2019).

[34] E. Smargiassi and P. A. Madden, Phys. Rev. B **49**, 5220 (1994).

[35] L.-W. Wang and M. P. Teter, Phys. Rev. B **45**, 13196 (1992).

[36] F. Perrot, J. Phys.: Condens. Matter **6**, 431 (1994).

[37] E. Chacón, J. E. Alvarellos, and P. Tarazona, Phys. Rev. B **32**, 7868 (1985).

[38] Y. A. Wang, N. Govind, and E. A. Carter, Phys. Rev. B **58**, 13465 (1998).

[39] Y. A. Wang, N. Govind, and E. A. Carter, Phys. Rev. B **60**, 16350 (1999).

[40] J. Xia and E. A. Carter, Phys. Rev. B **86**, 235109 (2012).

[41] W. Mi, A. Genova, and M. Pavanello, J. Chem. Phys. **148**, 184107 (2018).

[42] Q. Xu, Y. Wang, and Y. Ma, Phys. Rev. B **100**, 205132 (2019).

[43] J. Seino, R. Kageyama, M. Fujinami, Y. Ikabata, and H. Nakai, Chem. Phys. Lett. **734**, 136732 (2019).

[44] R. Meyer, M. Weichselbaum, and A. W. Hauser, J. Chem. Theory Comput. **16**, 5685 (2020).

[45] M. Fujinami, R. Kageyama, J. Seino, Y. Ikabata, and H. Nakai, Chem. Phys. Lett. **748**, 137358 (2020).

[46] S. Manzhos and P. Golub, J. Chem. Phys. **153**, 074104 (2020).

[47] J. Lindhard, K. Dan. Vidensk. Selsk., Mat.-Fys. Medd. **28**, 8 (1954).

[48] C. Covington, D. Kidd, H. Buckner, H. Appel, and K. Varga, Phys. Rev. E **100**, 053301 (2019).

[49] E. Runge and E. K. U. Gross, Phys. Rev. Lett. **52**, 997 (1984).

[50] K. Varga and J. A. Driscoll, *Computational Nanoscience: Applications for Molecules, Clusters, and Solids* (Cambridge University Press, Cambridge, UK, 2011).

[51] R. Jestädt, M. Ruggenthaler, M. J. T. Oliveira, A. Rubio, and H. Appel, Adv. Phys. **68**, 225 (2019).

[52] D. Kidd, A. S. Umar, and K. Varga, Phys. Rev. B **98**, 075108 (2018).

[53] N. T. Maitra, I. Souza, and K. Burke, Phys. Rev. B **68**, 045109 (2003).

[54] J. P. Perdew and A. Zunger, Phys. Rev. B **23**, 5048 (1981).

[55] C. Huang and E. A. Carter, Phys. Chem. Chem. Phys. **10**, 7109 (2008).

[56] J. P. K. Doye, J. Chem. Phys. **119**, 1136 (2003).

[57] K. Luo, J. I. Fuks, E. D. Sandoval, P. Elliott, and N. T. Maitra, J. Chem. Phys. **140**, 18A515 (2014).

[58] Q. Xu, J. Lv, Y. Wang, and Y. Ma, Phys. Rev. B **101**, 045110 (2020).